CYPRESS COUPLER FOR LIQUID CRYOGEN TRANSFER

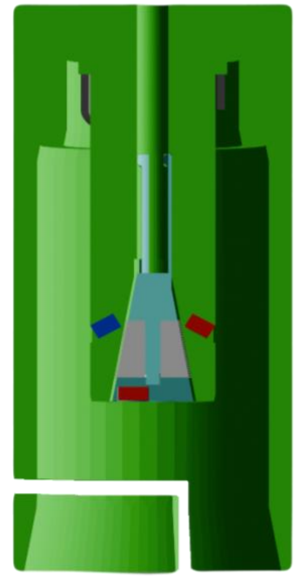

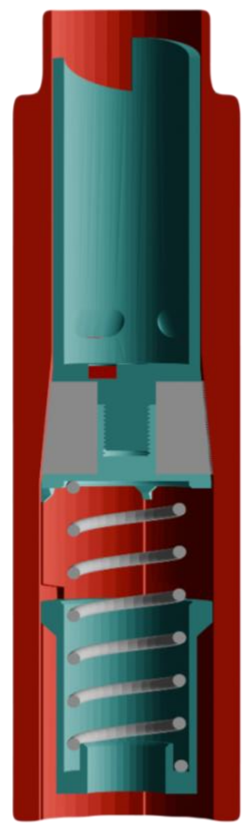

Washington State University

HYPER - CYPRESS Team Members:

Alexis Williams – Undergraduate – Mechanical Engineering

Reagan Dodge – Undergraduate – Mechanical Engineering

Adam Berg – Undergraduate – Mechanical Engineering

Justin Godin – Undergraduate – Mechanical Engineering

Kelson Peters – Undergraduate – Mechanical Engineering

Faculty Advisor:

Professor Jacob Leachman

Quad Chart

Washington State University CYPRESS Coupler

Theme Category, Major Objectives & Technical Approach

- Category - Automated Cryo-Couplers for Propellant Transfer
- Design coupler with the ability to safely and efficiently transfer cryogenic propellant.
- Intrinsically safe coupler design, allowing for minimal Personal Protective Equipment, and maximum propellant flow.
- Future testing with LN2 in partnership with NASA AFRC.
- Innovative polymer seals for cryogenics and light weight metal alloys.

Image/Graphic

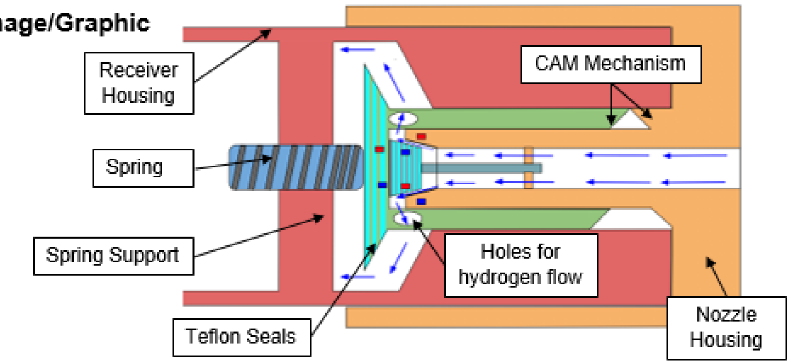

Key Design Details & Innovations of the Concept

- Multi-layered PTFE seals to provide reliable sealing at cryogenic temperatures and FOD resistance
- Al6061-RAM2 material provides lighter alternative to stainless steel with similar desirable thermal conductivity
- CAM lock method that employs the use of magnets to open and close the coupler.
- Simple two-motion operation procedure for ease of automation and integration into existing infrastructure.

Summary of Schedule & Costs for the proposed solution's path to adoption

- **TRL 1**- Literature Review Oct-24 – Dec 24
- **TRL 2**- Preliminary Design Development Dec 24 – Jan 25
  - Proposal Document Development Jan 25 – Mar 25
- **TRL 3**- Preliminary mechanisms testing Feb 25 – Apr 25
  - Technical Paper Development Apr 25 – Jun 25
- **TRL 4**- Preliminary Prototype testing with LN2 Jun 30 – Aug 15

Table of Contents

1. Summary Statement: CYPRESS – Novelty Born of Necessity

Cryogenic couplers currently under development require extensive purging, are cumbersome to handle, prone to leakage, and cost prohibitive. Utilizing cryogenic expertise from the HYdrogen Properties for Energy Research (HYPER) Center, the CYPRESS team addresses these issues by combining proprietary multi-layer flexible cryogenic polymer seals, NASA-developed 3D printed metal alloys, and NASA-proprietary magnet coupling technology to create a purge-less, safe, and resource-efficient Liquid Hydrogen (LH2) refueling coupler. The CYPRESS coupler is an intrinsically safe coupler meant for easy use that has not been seen in the industry to date. In Greek mythology, the cypress tree is associated with the goddess Artemis, representing life, growth, and renewal. CYPRESS (CrYogenic Performance REfueling Safety System) reflects the goals of the Artemis mission while highlighting the recent advances in cryogenic science.

The operational challenge solved by this project is the safe, quick, reusable temporary connection of liquid cryogen transfer lines. Our novel approach to couplers will address several issues relevant to cryogen transfer in terrestrial, lunar, and cis-lunar environments:

1. Loss of cryogen via environmental heat ingress, cooling of excessive thermal mass, and/or poor sealing at the cryogen-environment interface.
2. Need for extensive Personal Protective Equipment (PPE) and safety training for operators performing high-risk fluid transfers.

Our mitigation of the above issues will improve the safety of both human operators on Earth and astronauts in space, as well as improve the overall efficiency of the fluid transfer process.

Our proposed solution to this challenge is a hand-held coupling system that utilizes novel conformable sealing technology to reduce safety risks and leakage losses. Furthermore, additively manufactured aluminum alloys reduce cooling losses and introduce weight and cost savings over traditional stainless-steel materials. On Earth, thermal stand-offs and ergonomic handles allow an operator to safely transfer a contained flow of liquid cryogen between receptacles with a simple insert and twist operation, exhibiting a functionality like that of a traditional gas station for commercial vehicles. A specialized cam mechanism and magnetic lock inhibit the uncoupled flow of cryogen, tampering, or misalignment of the receiver and nozzle. The design is adaptable for astronaut use with handles designed to accommodate space suits. In a synergistic development with NASA's CryoMag team, our coupler can also be adapted for use in cis-lunar environments. The added risks of extravehicular activity (EVA) can be avoided by the addition of an actuation system that can open and close the coupler, likely requiring electrical input from one of the transferring vessels. Plugs or mechanical irises can be inserted into the nozzle and receptacles when not in use to limit lunar dust contamination of the sliding thermal standoff interfaces.

Initial design phases with total analysis of components and expected performance parameters have been completed during NASA HuLC 2025. Proof of concept prototyping has also been completed for the magnet actuation system and functionality of the coupler in a PLA prototype.

A partnership with NASA AFRC, the Cryomag team, and the Cryogenic Fluid Management team at NASA MSFC is underway beginning June 2nd through August 15th to move the concept through initial LN2 testing. This report details the numerical analyses performed and a complete design briefing.

A preliminary prototype may be produced using a nylon-carbon fiber composite for LN2 testing with the goal of reducing time and cost during initial phases. Additively manufactured polymer matrix composite LH2 fuel tanks have been previously developed at HYPER. Tanks made of polymer matrix composites reinforced with carbon fiber and glass beads showed no LH2 leakage unless the material had previously been compromised by unsealed or broken joints [14]. This finding supports the hypothesis that such additively manufactured materials may be used for a preliminary prototype. A final prototype would benefit from the added strength and durability of metals to withstand the loading conditions of a coupler over a long lifespan.

2. CYPRESS DESCRIPTION

The CYPRESS coupler prioritizes quick connection and minimization of error by reducing the coupling process to two motions. During the coupling process, cam surfaces and patterned magnets interact to actuate the poppet valves and allow for cryogen flow. The locations of the cam surfaces and patterned magnets are labeled in the (1) Uncoupled step of Figure 1 below. Cam surfaces at the end of the receiver poppet (left) and inside the nozzle housing (right) actuate the receiver poppet while patterned magnets embedded in each poppet and in the nozzle housing actuate the nozzle poppet. The interaction of these systems is further described below in reference to the process shown in Figure 1. The operational schematic shown in Figure 1 assumes that the receiver end is fixed in place as if integrated into a fuel system of a vehicle and the nozzle is free to move as if at the end of a flexible transfer line.

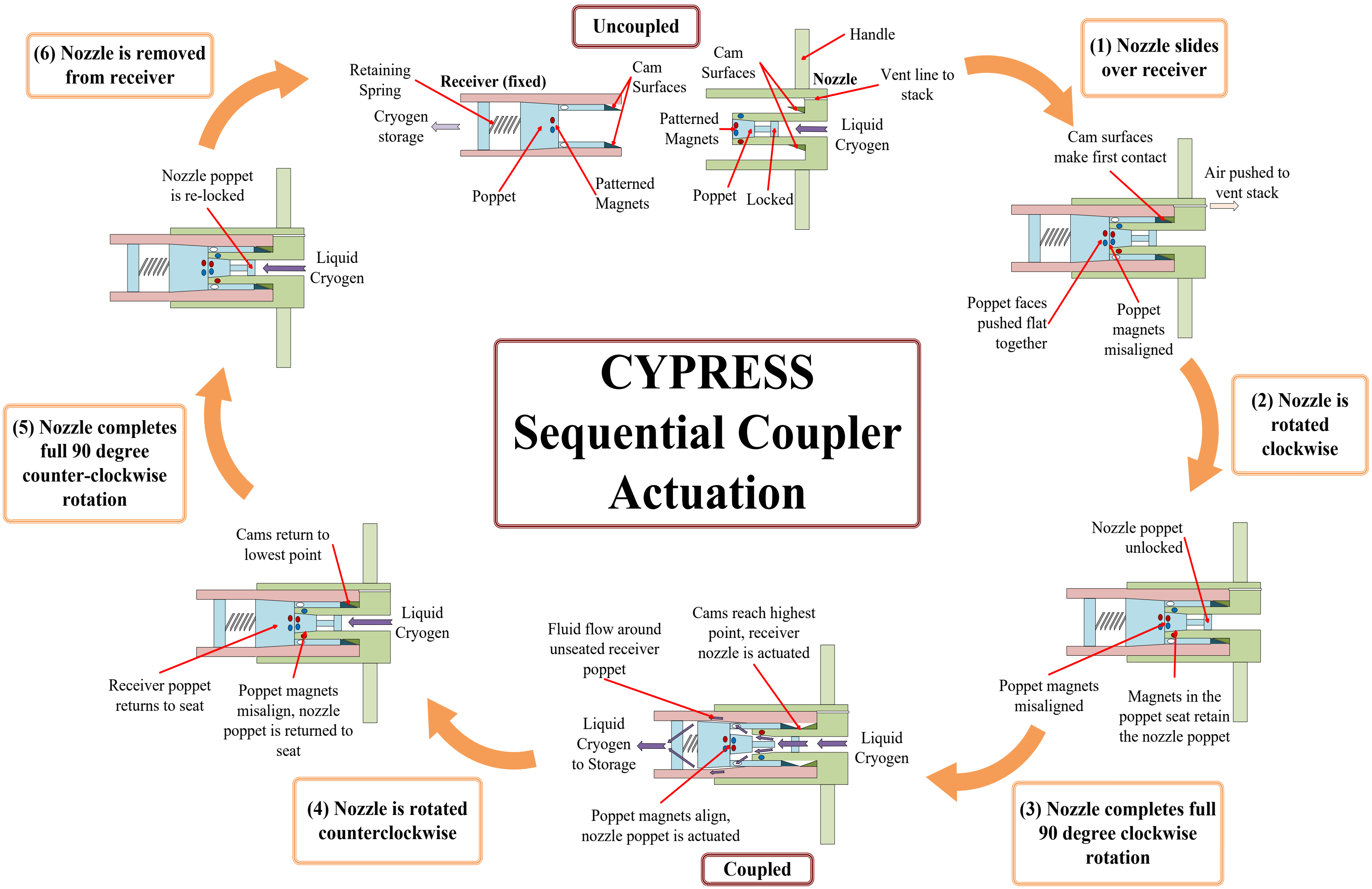

Figure 1. CYPRESS Sequential Coupler Actuation

The alignment of the nozzle and receiver is addressed in detail in the following Robotic Coupling subsection; Figure 1 above illustrates only the mechanical operation of the coupler and does not encompass alignment considerations. To begin flow, the nozzle is linearly inserted over the receiver, as shown in step (1) of Figure 1. At this step, air or other gaseous contaminants are redirected through a vent line at the back of the nozzle, eliminating the need for purging of the transfer volume. Also at this step, the cam surfaces make first contact and the magnets in the poppets are misaligned such that they do not attract each other. It should be noted here that a locking mechanism in the nozzle housing retains the nozzle poppet while uncoupled. During step (2), the nozzle is rotated clockwise. During the clockwise twist, magnets in each poppet align to rotate the nozzle poppet approximately 10°, disengaging the locking mechanism to allow for valve actuation. After this initial rotation, the poppet magnets remain aligned to hold the poppets together. Also during coupling, a guide track (not shown) at the outside of the nozzle housing is paired with a guidepost (not shown) on the receiver housing to restrict motion to only the required insertion and rotation. As the clockwise rotation is completed to a full 90° twist in step (3), the cam surfaces make contact at the highest point, pushing the receiver poppet out of its seat as the magnetic force between the poppets pulls the nozzle poppet out its seat. This unseating event opens the path for fluid flow through the gaps between the plug seals and the plug seats on either component, as shown in purple on the coupled step in Figure 1. Flow moves from right to the left, following an assumed pressure gradient from the high-pressure nozzle fluid to the low-pressure receiver side.

When the desired amount of cryogen has been transferred, the uncoupling process is initiated by a counterclockwise rotation of the nozzle as shown in step (4) of Figure 1. This rotation returns the cam surfaces to the lowest contact point as a retainer spring on the receiver and retaining magnets on the nozzle guide the poppets back to their respective seats. As the counterclockwise rotation is completed to the full 90° in step (5), the nozzle poppet is rotated the final 10°, engaging the poppet locking mechanism. Complete rotation in step (5) also misaligns the poppet magnets, removing the attractive force holding them together. Finally, the nozzle is removed from the receiver in a linear motion as shown in step (6) and the components return to the uncoupled state.

Robotic coupling in the absence of human-operators is just as easy due to the error-proofing features of the CYPRESS coupler. The nozzle side of the coupler will be mounted to the spacecraft via flexible hose with a small frame connecting a linear actuator and rotary actuator. Once two spacecraft dock together, most alignment that would be required for coupling has been accomplished. Now, our linear actuator extends the nozzle end and, using guiding chamfers and compliant mounting mechanisms on the receiver end, connects the two. Then the rotary actuator engages, rotating the nozzle end relative to the receiver end, opening our valves and allowing flow. On both actuators, current sensing will be used to determine when they have reached their endpoint. To decouple and stop flow, the reverse would happen, rotary actuator operates in the opposite direction, and the linear actuator then retracts the nozzle end. A prototype automated setup will include a small, desktop-sized frame housing both ends of the connector, with a mock linear actuator and rotary actuator.

Mass & Size estimates are based on the coupler not accounting for fittings, handles, or automation system. The nozzle assembly is 10” long by 4.5” in diameter and comes out to roughly 1.5 pounds. The receiver assembly is 15” long and comes out to roughly 3 pounds. While the main body of the receiver is 3.7” in diameter, the alignment pin makes the maximum diameter 4.5”.

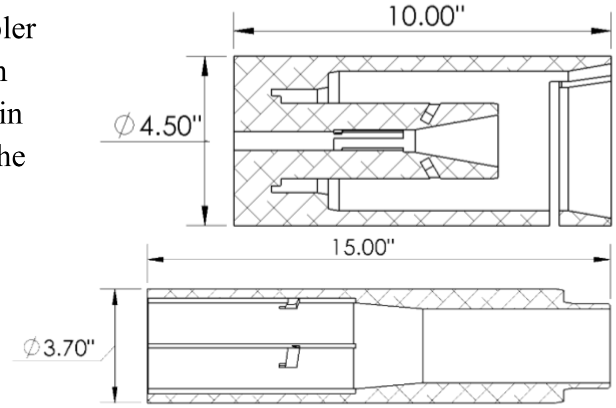

Figure 2. Outside dimensions of coupler sides

For lunar conditions, two dust mitigation systems have been considered. A removeable dust cover on the ends of the nozzle also functions as a thermal standoff, preventing contact with the cold end and containing any leaking cryogen to the vent ports in the case of a failed seal. This system would prevent the abrasive effects of regolith dust on mechanical surfaces that plagued the Apollo missions [4]. Polytetrafluoroethylene (PTFE) multi-surface seals have shown potential Foreign Object Debris (FOD) resistance in initial testing with A4 Course Arizona Test Dust [5]. Mt. St. Helen’s ash was used as a lunar dust simulant and showed similar behavior to the Arizona Test Dust [11]. Purge functionality may be added to the coupler to utilize the Leidenfrost effect as the cryogen boils off to remove dust from mechanical surfaces prior to coupling to reduce friction and wear on the components while ensuring a close seal.

3. New Technology Overview

Conformable plugs like that shown in Figure 3 have demonstrated cryogenic sealing in pressure relief valves (PRVs). Stacked layers of PTFE discs and spacer rings create redundant sealing surfaces that exhibited significantly less leakage at 77 K and during foreign object debris testing than commercial off-the-shelf PRVs [5]. This concept has been adapted to the CYPRESS poppets to provide cryogenic sealing at the end of a transfer line.

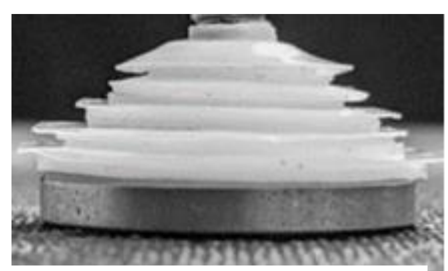
Figure 3. Previously demonstrated conformable plug seal [5]

Each poppet is comprised of solid PTFE, PTFE discs and spacer rings, and samarium cobalt (SmCo) magnets. The nozzle poppet is shown on the left in Figure 4 below, while the receiver poppet is shown on the right.

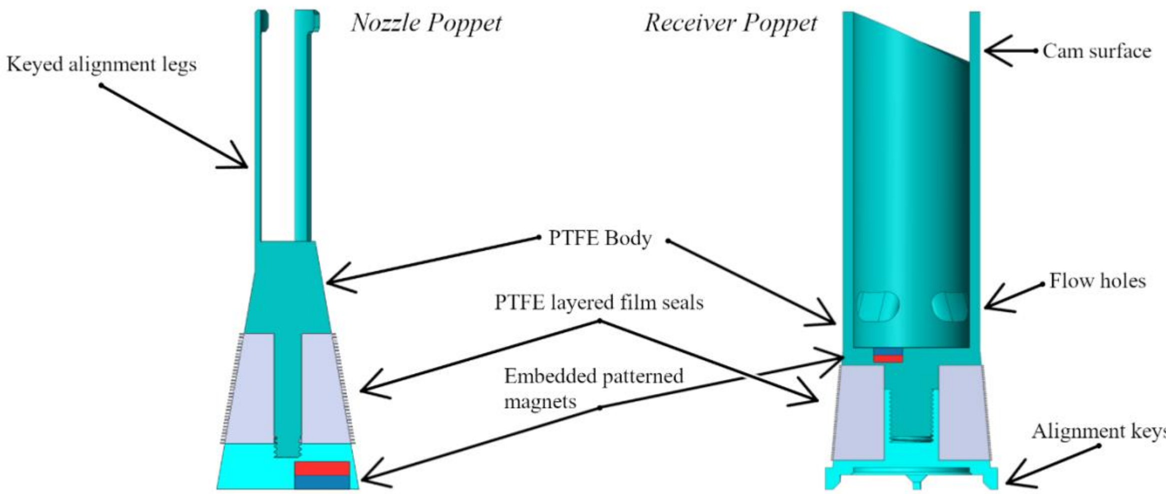

Figure 4. Poppet cross-sections

Aluminum 6061-RAM2 is a high-strength aluminum alloy for which NASA and industry partners previously developed laser powder directed energy deposition (LPDED) additive manufacturing [7]. According to thermal conductivity testing conducted at HYPER, Al6061-RAM2 displays a thermal conductivity [6] on the same order of magnitude as stainless steel (SS) 316 at 20 K [9]. SS 316 is generally used in cryogenic applications due in part to its low thermal conductivity, which slows heat ingress and thus slows cryogen boil off. Al6061-RAM2 has 1/3 of the density of SS 316 and requires less than 2/3 the amount of LH2 to be completely cooled, as shown in Appendix B. Al6061-RAM2 introduces weight and cryogen savings that ultimately improve coupler performance.

4. Verification & Validation

Heat transfer must be considered in the design of cryogenic components for use in terrestrial conditions to avoid water icing or liquid air formation. Water ice poses a blockage risk that may prevent proper coupling and fluid transfer while liquid air is classified as a flammable mixture that may pose risks to operators or surrounding infrastructure. The CYPRESS coupler incorporates thermal standoffs and inherent vacuum jacketing to mitigate these risks. Minimization of heat transfer paths through the housing and poppet materials constitute thermal standoffs which resist the flow of heat. Inherent vacuum jacketing is formed by trapped argon gas in void spaces during the LPDED manufacturing process of each housing component. This argon autogenously generates vacuum when the nozzle is cooled. Moreover, aluminum has a very low diffusion coefficient such that vacuum re-purging will not be required over the coupler lifetime. Critical areas for the formation of water ice or liquid oxygen include the exposed nozzle poppet surface and the nozzle valve seat, as noted on the diagram in Figure 5 below. The receiver poppet surface and receiver valve seat can also be analyzed using the procedure described below.

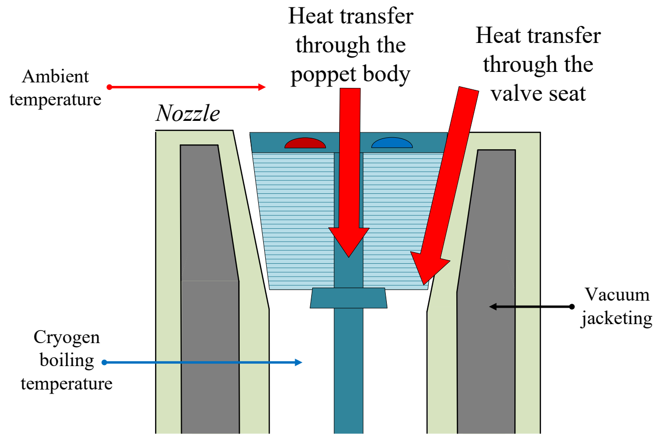

Figure 5. Heat transfer paths

Conduction through the valve seat was determined using Fourier's Law and the estimated thermal convection from the environment to the component at standard conditions. On the nozzle side, the thermal convection, Q, into the component was estimated using equation (1) below where $A_{surface}$ represents the exposed surface area, ΔT is the desired thermal gradient from ambient 300 K to the standard freezing point of water 273 K, and the convective heat transfer coefficient, h, was set at 5.0 W/m^2 for natural convection.

$$Q = hA_{surface}\Delta T \tag{1}$$

The convective heat transfer, Q, calculated from equation (1) above was then used to determine the length, L, of the poppet valve seat using the modified Fourier's Law described in equation (2) below. Where ΔT is the expected thermal gradient across the seat from 273 K to the standard boiling point of LH2 at 20 K, k is the integrated average thermal conductivity over the expected temperature gradient, A_{avg} is the average cross-sectional area of the angled seat, and L is seat length. Based on similarities between the thermal conductivity of Al6061-RAM2 and SS304 described in Section 3 and a lack of information available on the aluminum alloy in literature, k was taken to be equivalent to that of SS304 across the same temperature range. The thickness of the valve seat walls was taken to be 1 mm, the minimum capability of available LPDED printing, to minimize A_{avg} and resist heat transfer.

$$Q = \frac{kA_{avg}\Delta T}{L} \tag{2}$$

Analyses described above determined the designed dimensions of the valve seats for each component, yielding a poppet length of 2 inches on the receiver side and 2.25 inches on the nozzle side.

To verify the no-icing condition at the poppet surfaces, heat transfer from convection to the poppet face and conduction through the poppet body were analyzed using the poppet length determined by the valve seat. This analysis followed a similar process to that of the valve seat, estimating the thermal convection to the poppet surface and conduction through the poppet body. To account for the changing thermal conductivity over the expected temperature range, an integrated average thermal conductivity of 0.248 W/m-K for PTFE from 273 K to 20 K [15] was used. First calculating the thermal convection to the poppet face and then solving for the surface temperature using a thermal resistance network for each poppet yielded surface temperatures around 300 K, above the 273 K icing limit. Using this method, the heat leak into the cryogen through the poppet body was an estimated 0.7 W for each component.

For analysis of the valve seat, conduction through the material is assumed to be much higher than the heat transfer through the vacuum jacketing, thus transfer through the jacket may be neglected. However, the actual heat transfer through the argon gas jacket and heat leak to the cryogen through the walls of the component housing can be estimated from the expected pressure within the voids at cryogenic steady-state and the thermal conductivity of argon gas. Before chill-in, the pressure inside the argon voids is conservatively assumed to be equal to atmospheric pressure based on the LPDED printing conditions. The pressure at ambient conditions may be lower due to high temperatures at the print site, though the LPDED process describes standard conditions within the print volume [7]. Using the initial condition of standard temperature and pressure, an estimate of the vapor pressure in the void spaces after cooldown to 20 K can be made. During the cooldown process with liquid hydrogen, the argon is cooled below its melting point of 83.81 K. Below this temperature, the argon solidifies within the void space and the pressure in the insulation jacketing is equivalent to the sublimation pressure of solid argon at 20 K, lower than 10^{-5} Pa [19]. This pressure constitutes a high vacuum and falls within the generally accepted definition of vacuum insulation [15]. The effective thermal conductivity for vacuum insulation in the high vacuum regime at 10^{-3} Pa is 10 mW/m-K has previously been measured [20]. Though the thermal conductivity of argon gas is significantly lower than that of air and the expected pressure in the voids is below 10^{-3} Pa, this thermal conductivity value has been selected to provide conservative estimates of heat transfer through the insulation layer. A resistive thermal network based on the dimensions shown below in figure 6 was analyzed.

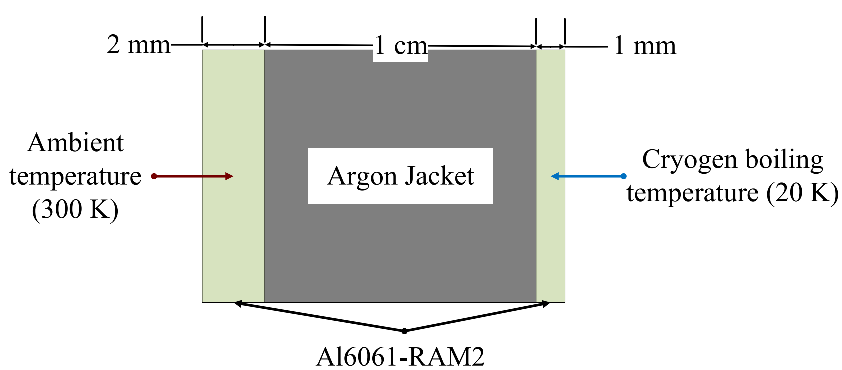

Figure 6. Dimensions of the insulated wall

The 1 cm thickness of the argon jacket was selected for significant thermal resistance with minimal increase of component size. Using the thermal conductivity measurements for Al6061-RAM 2 at ambient conditions for the outer wall and at 20 K for the inner wall, a thermal resistance network was analyzed which estimated a heat leak of 7.8 W from the environment to the cryogen along the 6-inch pipe length of each component.

Summation of the heat transfer through the poppet and insulation yields a total expected heat ingress in the uncoupled state of approximately 8.5 W for each component. This value is within the range for heat ingress of a standard bayonet coupler of comparable size which receives an estimated 8.8 W of heat leak in the coupled state [21].

Magnets and cam systems work together to actuate the valves of the CYPRESS coupler. On a basic level, it utilizes two stationary disc arrays on the nozzle end, and one disc array that rotates relative to the other two on the receiver end. The purpose of the back array on the nozzle end is to provide the sealing force necessary to prevent hydrogen leakage by providing an attractive force to the array on the valve. The purpose of the receiver array is to at first provide little to no force on the nozzle arrays, and then as rotated, create a greater attractive force. Once the sealing force is overcome, the valve opens, and fluid flow is allowed. On decoupling, the reverse happens where the array no longer overcomes the sealing force, and the valve is then closed.

Each array is designed to approximate what a printed magnet could do, though with less precision.

To understand the movement of the valve, the forces between each array and the magnets within must be analyzed. This is generally modeled as the product of their strengths divided by the distance apart squared.

$$F = \frac{S_1 * S_2}{D^2} \tag{3}$$

The force of each magnet on any single magnet in the valve’s array can then be determined based on their distances apart along their line of action. However, to translate these separate forces into the force opening and closing the valve, the axial component of each is required. This can be found using the relation of the length of the line of action (D) to the distance apart axially (x).

$$F_{axial} = F * \frac{x_2 - x_1}{D} \tag{4}$$

Once all the individual forces acting on the valve array have been found, they must be corrected for polarity. Magnets of the same polarity repel, magnets of the opposite polarity attract, forming the correlation below.

	Positive	Negative
Positive	-	+
Negative	+	-

This relationship was then turned into an equation to work for every force and sums all the forces from one array interacting on the valve's array

$$F_{aggregate} = \sum_{j=1}^{n_j} \sum_{i=1}^{n_i} F_{ij\ axial} * -1 * P_j * P_i \tag{5}$$

Where n_j is the number of magnets in the valve array, n_i is the number of magnets in the interacting array, P_i is the polarity of the interacting magnet, and P_j is the polarity of the valve magnet.

Now all the forces from the interacting arrays must be combined. This approach has not accounted for the fact that the valve magnets have one polarity on one side and the opposite polarity on another. As such, rather than adding, they are subtracted.

$$F_{valve} = F_{aggregate\ 1} - F_{aggregate\ 2} \tag{6}$$

This does not fix the magnets in reality; however, it is as simple as flipping the magnets in one of the interacting arrays for proper actuation.

Now that the force on the valve at a position can be determined, we programmed a Python code that numerically solves for the position of the valve starting from the coupler being put together and then rotated open, including the action of the cam surface separating the arrays apart.

In creation of the array setup used in the CYPRESS coupler, the strengths of each magnet were set equal. This assumption allows us to build an array with any set of magnets, so long as they are the same, and avoids making any assumptions about the relative strengths between different magnet shapes.

Opening force required to actuate the coupler was determined at a design pressure of 80 psi based on common cryogen storage pressures. Unfurling the cam into a 2D ramp, the force required to push the valve open (F_t) was calculated based on the distance the valve opens (Δx), circumferential length of the cam (L), and the force from fluid pressure (F_p). This assumes that said force will substantially drop once the valve begins to open and the pressure across the valve equalizes. It also does not account for friction, the torque applied by the magnets, nor the preload force from the spring. As such, it should be treated as a lower bound.

Then, with the force required to open, equation (11) can be used to find the radius of the handle based on the desired applied force, or vice versa.

It was found that with an applied force of 24 lbs, the handle will need to be 5.77” in radius. For automated use, it was found that using a 2.5” radius pitch circle, our radial actuator’s output gear must produce a force of at least 55.40 lbs.

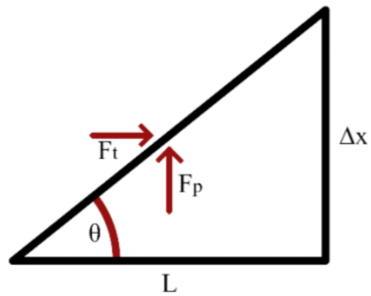

$$F_p = P * \pi * \left(\frac{D_{valve}}{2}\right)^2 \quad (7)$$

$$L = \frac{\emptyset}{360} * 2\pi * \frac{D_{cam}}{2} \quad (8)$$

$$\theta = \tan^{-1}\left(\frac{\Delta x}{L}\right) \quad (9)$$

$$F_t = F_p * \tan(\theta) \quad (10)$$

$$R = \frac{F_t}{F_{Applied}} * \frac{D_{cam}}{2} \quad (11)$$

Cam wear expectation after an extended number of coupling cycles can be estimated using the wear equation shown below, see tables 12-8,10,11 from [18].

$$Wear = Motion\ Factor * Environ\ Factor * Wear\ Factor * Pressure * Velocity * Time$$

Motion Factor:	1.3
Environmental Factor:	6
Material Wear Factor:	$1.3 * 10^{-9}$

Assumptions necessary are as follows: an opening and closing velocity of 10 ft/min, cycle time of 1 min, 10,000 cycles, and a material properties place holder of (66 Nylon + 15% PTFE). With our input of 80 psi the result we found after 10,000 opening and closing cycles is **0.002 $\boldsymbol{in^3}$** of material worn away. Now having a face-to-face total surface area of 0.893 in^2 the y-displacement change due to wear would be **0.002 *in.***

Pressure vessels must comply with ASME BPVC VIII-1 which calls for a minimum factor of safety of 3.5 for hoop and axial stresses [16]. This condition should be checked for the walls holding the cryogen under pressure as well as the walls holding the low-pressure argon. The inner walls holding the cryogen under pressure meet the condition for thin-walled pressure vessels described by equation (7) below where t is the 1 mm thickness of the wall and r is the 6.4 mm inner radius.

$$t < 10r \quad (7)$$

Hoop stress, σ_h, in the thin-walled pressure vessel is calculated using equation (8) below where P is the pressure difference across the wall. At the wall between the pressurized cryogen and the argon jacketing, the differential is given by subtracting the low-pressure argon jacketing value from the high-pressure cryogen value.

$$\sigma_h = P * \frac{r}{t} \tag{8}$$

Using a cryogen pressure of 80 psi and argon vapor pressure of 10^{-5} Pa, the hoop stress is 500 psi. The designed factor of safety for a pressure vessel is given by the ratio between the hoop stress and the yield stress. Taking the yield stress of Al6061-RAM2 to be 45000 psi [17], the factor of safety in the wall is 90, exceeding the 3.5 requirement from general pressure vessel codes.

5. Path-to-Flight Timeline (Full Concept & Mission Architecture Timeline)

In the scope of this competition, the team has iterated through the following TRL to advance CYPRESS for use in the Artemis missions:

TRL 1: Basic principles: Teflon seals used in cryogenic applications, Al6061-RAM2 thermal conductivity and density properties observed.

TRL 2: Technology concept development: CYPRESS coupler was developed after several paradigm iterations and a conceptual design review. The benefits of several paradigms were combined to create the final technology.

TRL 3: Function proof of concept: CYPRESS coupler was 3D printed with polymers to demonstrate size, shape, and design. This testing verified the viability of the design from the user experience standpoint. Calculations and modeling were also completed to demonstrate ability of the coupler to handle cryogenic fluids.

All above development was completed at Washington State University Pullman campus through the Hydrogen Properties for Energy Research (HYPER) center and the Mechanical Engineering capstone project process.

As the development of CYPRESS continues through the TRL process, testing will continue at NASA Armstrong Flight Research Center (AFRC) with support from the Cryogenics Fluid Management department at NASA Marshall Space Flight Center and will be done by three members of this team in the next three months. This testing will iterate through the following TRL:

TRL 4: LN2 testing and validation: Functionality, including sealing capabilities, heat ingress, pressure drop, and surface icing with LN2 flow will be assessed. This testing will demonstrate the viability of the coupler in cryogenic applications.

TRL 5: LH2 testing and validation: Functionality testing will be repeated with LH2 to demonstrate viability of the coupler with liquid hydrogen.

Due to schedule and budget constraints, further testing will be needed prior to completion of the testing done at AFRC to progress beyond TRL 5. This testing should include the effect of potential contaminants, such as lunar dust, on the coupling mechanism, testing of the coupler in a relevant environment, including cold conditions and a vacuum, and testing to verify the coupler's resilience to flight loads. Testing of the automation mechanism will also need to be completed to verify the coupler's use in situations that require complete autonomy. Finally, durability testing will need to be completed and the lifespan of the coupler will need to be determined. All of this testing will take place in the next two years in order to be prepared for implementation in the Artemis missions in the three to five year time window.

6. Budget Assessment

Below is a summary of the budget for this project. Concept development and prototyping for the scope of the HuLC competition is covered in Phase 1. Phase 2 details the further testing that will be completed at NASA Armstrong by three team members this summer to develop the concept into a viable product for use in the Artemis missions.

PI Name(s): Jacob Leachman							**PHASE 1**	**PHASE 2**	**TOTAL**
Agency Name: NASA							**04/08/25 06/01/25**	**06/02/25 08/08/25**	
00 - SALARIES	**Pay Rate**	**# Mos.**		**% FTE**		**Salart**			
PI: Jacob Leachman	0.00	0.00		0.00%		31.30%	-		-
PI: Emily Larsen	0.00	0.00		0.00%		31.30%	-		-
01 - WAGES	**$ Per Hr.**	**Hrs/Wks**		**# Wks.**					
Student:	$0.00	0		0		**Wages**	-		-
					Benefits	2.9%	-		-
07 - BENEFITS									
						Total Salaries/Wages/Benefits	-		-
02 - PURCHASED SERVICES (Personal Services Contracts and Consultants and Computer Services)									
						Total Personal Services Contracts	-		-
03 - GOODS/SERVICES (Including Small/Attractive Items)									
Conference registration							2,600		2,600
						Total Goods/Services	2,600		2,600
04 - TRAVEL									
Travel to Competition							3,625		3,625
						Total Travel	3,625		3,625
05 - COMPUTER SERVICES									
						Total Computer Services	-		-
06 - MATERIALS AND SUPPLIES									
						Mechanism Testing Supplies	300	-	300
						Cryogenic Testing Supplies and Manufacturing	-	15,000	15,000
						Total Materials and Supplies	300	15,000	15,300
08 - SCHOLARSHIPS AND FELLOWSHIPS (SUBSIDIES/PARTICIPANT SUPPORT COSTS)									
Remaining Scholarship funds							2,725		2,725
NASA Internship Stipend (3 interns)								32,800	32,800
						Total Stipends/Subsidies/Participant Support Costs	2,725	32,800	35,525
14 - AWARD RESTRICTIONS (RESTRICTED: incl. SUBAWARDS/SUBCONTRACTS)									
						Total Subcontracts/Restricted	-		-
TOTAL DIRECT COSTS							-		-
EXCLUSIONS									
Other (Off-Site Rental & Stipends, Etc)							-		-
						Total Exclusions	-		-
MTDC BASE						**Base**	-		-
13 - FACILITIES & ADMINISTRATIVE COSTS (F&A, IDCs, OVERHEAD)					**F&A Rate:**	**0.000%**	-		-
TOTAL COSTS							9,250	47,800	57,050

7. Conclusions & Key Findings

Rapid and safe transfer of cryogenic fuel is a critical aspect of humanity's return to the moon and journey deeper into the universe. The CYPRESS coupler offers a solution to automated terrestrial, cis-lunar, and lunar transfers utilizing revolutionary technologies in cryogenic fuel management. Operational simplicity eases the integration of CYPRESS into already existing infrastructure supporting the upcoming Artemis missions. Through NASA HuLC 2025, the CYPRESS coupler has been developed through the conceptual phases. Collaborations with NASA teams are supporting testing and validation to bring CYPRESS and humanity to the future of space exploration.

8. APPENDIX A: REFERENCES

[1] Hansen, Hans C, et al. *Cryogenic Fluid Management Technologies Enabling for the Artemis Program and Beyond*, ntrs.nasa.gov/api/citations/20205008297/downloads/ASCEND - CFM Technologies for Artemis Paper 2020-10-06 Final.pdf. Accessed 19 Feb. 2025.

[2] Bean, Paul, et al. *Magnetic Subsystem Design and Testing for the NASA Magnetic Latching Cryogenic Coupler*, ntrs.nasa.gov/api/citations/20220018468/downloads/20220018468FINAL_edited.pdf. Accessed 20 Feb. 2025.

[3] *CROSS-PROGRAM DESIGN SPECIFICATION FOR NATURAL ENVIRONMENTS (DSNE)*, National Aeronautics and Space Administration, ntrs.nasa.gov/citations/20210024522. Accessed 19 Feb. 2025.

[4] Stubbs, T J, et al. "Impact of Lunar Dust on the Exploration ..." *Lunar and Planetary Science XXXVI*, NASA, 2005, ntrs.nasa.gov/api/citations/20050176031/downloads/20050176031.pdf. Accessed 21 Feb. 2025.

[5] Wood, M, and J W Leachman. *Development of Conformable Cryogenic Valve Seats for Resilience to Foreign Object Debris*, IOP Publishing, 2024, Accessed 21 Feb. 2025.

[6] Shenton, M, et al. *Thermal Conductivity Measurements for Additively Manufactured AlSi10Mg and Al6061-RAM2 Aluminum Composites at Cryogenic Temperatures*, IOP Publishing, 2024, iopscience.iop.org/article/10.1088/1757-899X/1301/1/012171/pdf. Accessed 21 Feb. 2025.

[7] Fedotowsky, Tessa M, et al. *Al6061-RAM2 Development and Hot-Fire Testing Using Additive Manufacturing Laser Powder Directed Energy Deposition for Liquid Rocket Engine Channel-Cooled Nozzles*, National Aeronautics and Space Administration, Jan. 2024, ntrs.nasa.gov/api/citations/20230018090/downloads/AIAA%20Al6061-RAM2%20Nozzle%202023_Fedotowsky.pdf. Accessed 22 Feb. 2025

[8] Watson-Morgan, Lisa, et al. *NASA's Initial and Sustained Artemis Human Landing Systems*, ntrs.nasa.gov/api/citations/20205008849/downloads/final HLS IEEE paper.pdf. Accessed 22 Feb. 2025.

[9] Ekin, Jack W. *EXPERIMENTAL TECHNIQUES FOR LOW-TEMPERATURE MEASUREMENTS: Cryostat Design, Material Properties, and Superconductor Critical-Current Testing*, Oxford University Press, 2006, www.researchmeasurements.com/figures/ExpTechLTMeas_Apdx_English.pdf. Accessed 23 Feb. 2025.

[10] Lee, Jonathan A. *Hydrogen Embrittlement*, National Aeronautical and Space Administration, Apr. 2016, ntrs.nasa.gov/api/citations/20160005654/downloads/20160005654.pdf. Accessed 24 Feb. 2025.

[11] Wells, I, et al. *Lunar Dust Removal and Material Degradation from Liquid Nitrogen Sprays*, Acta Astronautica, 2023, https://doi.org/10.1016/j.actaastro.2023.02.016. Accessed 26 Feb. 2025.

[12] Crass, Aileen. "Why Machine When You Can Injection Mold." *Performance Plastics*, 27 Nov. 2024, performanceplastics.com/blog/teflon-why-machine-when-you-can-injection-mold/. Accessed 26 Feb. 2025.

[13] "Additive Manufacturing with Fully Fluorinated Polymers." *3M*, 2017, multimedia.3m.com/mws/media/1453204O/brochure-additive-manufacturing-or-3d-printing-with-fully-fluorinated-polymers.pdf. Accessed 26 Feb. 2025.

[14] Boettner, D. P. (2022). Experimental analysis of cryogenic hydrogen leakage in additively manufactured hydrogen tanks (Order No. 29256794). Available from Dissertations & Theses @ Washington State University WCLP; ProQuest Dissertations & Theses A&I. (2730324852). Retrieved from https://www.proquest.com/dissertations-theses/experimental-analysis-cryogenic-hydrogen-leakage/docview/2730324852/se-2

[15] A. L. Slotwinski, et al. *Characterization of Metal Powders Used for Additive Manufacturing.* National Institute of Standards and Technology, 2014, https://tsapps.nist.gov/publication/get_pdf.cfm?pub_id=907540. Accessed 26 Feb. 2025.

[16] *ASME Boiler and Pressure Vessel Code, Section VIII, Division 1: Rules for Construction of Pressure Vessels.* ASME, 2025. Print.

[17] *A6061-RAM2 Aluminum Alloy Data Sheet.* Elementum 3D, 18 Jan. 2024, https://www.elementum3d.com/wp-content/uploads/2024/02/A6061-RAM2-2-pg-Web-Event-Data-Sheets-2024-01-18.pdf. Accessed 26 Feb. 2025.

[18] Budynas, Richard G., and J. Keith Nisbett. *Shigley's Mechanical Engineering Design.* 10th ed., McGraw-Hill Education, 2015. See Tables 12-8, 12-10, and 12-11.

[19] Maltby, Tage W., Morten Hammer, and Øivind Wilhelmsen. "Equation of State for Solid Argon Valid for Temperatures up to 300 K and Pressures up to 16 GPa." *Journal of Physical and Chemical Reference Data*, vol. 53, no. 4, 2024, p. 043102. https://pubs.aip.org/aip/jpr/article/53/4/043102/3327141/Equation-of-State-for-Solid-Argon-Valid-for. Accessed 17 May 2025.

[20] Fesmire, James E., and Adam M. Swanger. *Advanced Cryogenic Insulation Systems.* NASA Kennedy Space Center, Aug. 27, 2019. NASA Technical Reports Server, https://ntrs.nasa.gov/api/citations/20190030314/downloads/20190030314.pdf.

[21] Flynn T M 2005 *Cryogenic Engineering* (Boca Raton: CRC Press)

9. Appendix B: Tables and Calculations

11 Thermal Properties

11.1 Thermal Conductivity (ASTM 1461)

The thermal performance of A6061-RAM2 has been evaluated using the laser flash method. For this method, differential scanning calorimetry (DSC) is used to calculate heat capacity, measured directly using a reversing heat capacity method. The heat capacity, along with thermal diffusivity and density of the material, is used to calculate thermal conductivity. Thermal diffusivity is measured using the laser flash method, where the front side of a sample surface is pulse heated with a short laser pulse and the time evolution of the back surface temperature is measured using an infrared detector. This generates a temperature profile curve tailored using an ID heat flow model from which the thermal diffusivity is extracted. The results of this test for a A6061-RAM2 HIP & T62 sample printed in an EOS M290 printer is provided in **Table 11.1**.

Table 11.1: Thermal conductivity of one A6061-RAM2 HIP & T62 sample printed on an EOS M290 .

Temperature		Specific Heat	Thermal Diffusivity	Thermal Conductivity	
°C	°F	J/g·K	mm^2/sec	W/m·K	$BTU \cdot in/hr \cdot ft^2 \cdot °F$
25	77	1.05	66.2	188	1300
40	104	1.14	66.5	204	1417
60	140	1.15	66.8	204	1411
80	176	1.13	67.3	200	1387
100	212	1.17	67.4	208	1440
120	248	1.17	67.6	206	1426
140	284	1.22	67.7	218	1512
160	320	1.22	67.8	217	1504
180	356	1.23	67.8	218	1514

Table 1: Elementum 3D Al6061-RAM2 Thermal Properties

Table 9.1: Tensile properties at different testing temperatures. All samples built on an EOS M290 using 40 µm layer thickness parameters and tested in the T61 condition. Each value represents an average ± one standard deviation.

Layer Thickness & Condition	Test Temperature (°C)	Number of: Samples	Lots	Builds	Printers	Ultimate Tensile Strength (ksi)	0.2% Offset Yield Strength (ksi)	Elongation (%)
40 µm, T61	-167	8	1	1	1	60.7 ± 1.5	54.8 ± 1.6	15.1 ± 0.8
	-100	8	1	1	1	56.5 ± 1.5	52.2 ± 1.8	13.0 ± 0.8
	-50	8	1	1	1	53.2 ± 2.5	49.5 ± 2.5	13.1 ± 0.6
	25	75	7	17	3	48.9 ± 2.5	46.4 ± 2.9	12.7 ± 1.8
	100	8	1	2	1	48.0 ± 0.7	46.5 ± 1.0	14.5 ± 0.8
	150	8	1	2	1	41.6 ± 0.8	41.4 ± 0.7	18.4 ± 2.5
	200	8	1	2	1	31.3 ± 1.3	31.0 ± 1.2	22.0 ± 6.9
	250	8	1	2	1	20.0 ± 2.2	17.4 ± 0.8	29.6 ± 5.0
30 µm, HIP & T62	-160	4	-	-	-	63.8 ± 0.5	52.1 ± 0.8	18.0 ± 0.0
	25	22	1	1	1	50.5 ± 0.9	44.0 ± 1.4	12.9 ± 1.1
	100	4	-	-	-	45.4 ± 0.9	42.9 ± 1.1	18.3 ± 0.5
	200	4	-	-	-	29.2 ± 1.8	29.1 ± 1.8	34.5 ± 2.4
	300	4	-	-	-	7.8 ± 0.4	7.2 ± 0.3	73.8 ± 3.0
	400	4	-	-	-	2.6 ± 0.3	2.4 ± 0.2	72.7 ± 19.6

Table 2: Al6061-RAM2 Tensile Properties at Cryogenic Temperatures

A1.6b Cooling power data: Amount of cryogenic fluid needed to cool common metals [a,b] *(Sec. 1.2)*

Cryogenic Fluid:		^4He (T_b = 4.2 K)		H_2 (T_b = 20.3 K)		N_2 (T_b = 77.3 K)
Initial Temp. of Metal:		300 K [L/kg]	77 K [L/kg]	300 K [L/kg]	77 K [L/kg]	300 K [L/kg]
Using the latent heat of vaporization only	Aluminum	58	2.6	5.4	0.25	1.01
	Copper	27	1.8	2.4	0.17	0.46
	Stainless Steel	30	1.2	2.8	0.12	0.54
Using both the latent heat and the enthalpy of the gas	Aluminum	1.60	0.22	1.03	0.14	0.64
	Copper	0.80	0.15	0.51	0.092	0.29
	Stainless Steel	0.80	0.10	0.52	0.064	0.34

T_b is the boiling temperature at atmospheric pressure.
[a] Determined from data by J. B. Jacobs (1962), *Adv. Cryog. Eng.* **8**, 529.
[b] For temperature combinations other than those given in this table, see Jacobs (1962, reference above).

Table 3: Cooling Power table for common metals [9]

Cooling power calculations:

For Al6061-RAM2 (assuming similar values as Aluminum):

$$Cooling\ Power = 2.5219\ kg * 5.4\frac{L}{kg} = 13.618\ L\ H_2\ to\ cool$$

For stainless steel:

$$Cooling\ Power = 7.3632\ kg * 2.8\frac{L}{kg} = 20.617\ L\ H_2\ to\ cool$$